Fully unconstrained non-collinear magnetism in triangular Cr and Mn monolayers and overlayers on Cu(111) substrates

D Hobbs†‡ and J Hafner†

† Institut für Materialphysik and Centre for Computational Material Science, Sensengasse 8/12, A-1090 Wien, Austria
‡ Institut für Theoretische Physik, Technische Universität Wien, Wiedner Hauptstraße 8-10/136, A-1040 Wien, Austria

Abstract. A recently developed fully unconstrained approach to non-collinear magnetism has been applied to the investigation of the magnetic ground state of triangular free-standing Cr and Mn monolayers and overlayers on Cu(111) substrates. Such systems represent a physical realization of a frustrated two-dimensional antiferromagnet. We find that the ground state of the Cr monolayers is non-collinear; it shows $\sqrt{3} \times \sqrt{3}$ periodicity with $\pm 120°$ angles between the directions of the magnetic moments on neighbouring sites. Mn monolayers on the other hand have a collinear ground state with antiferromagnetically coupled rows and c(2×2) periodicity. The fully unconstrained description allows for a detailed investigation of the spin densities in the interstitial regions.

1. Introduction

One of the simplest examples of a frustrated two-dimensional spin system, where no perfectly collinear magnetic arrangement can be accommodated, is the antiferromagnetic planar (XY-) model with nearest-neighbour interactions on a triangular lattice. Lee *et al* [1] have conducted an extensive study of these systems using group theoretical symmetry arguments combined with Monte Carlo simulations and a detailed finite-size scaling analysis. Antiferromagnetic inter-actions are a source of magnetic frustration on the triangular lattice. The ground states of such systems tend to consist of spins ordered on three interpenetrating sublattices with lattice vectors of length $\sqrt{3}a$ while spins on different sublattices are orientated at $\pm 120°$ to each other. Earlier, Wannier [2] had proved that by considering the ground-state energy of any single elementary triangle and minimizing the energy with respect to two of the spin angles, one obtains ground states for the triangle in which the spins form $\pm 120°$ angles. This argument is then generalized to the $\sqrt{3} \times \sqrt{3}$ lattice and shows that the ground state can have only $\sqrt{3} \times \sqrt{3}$ periodicity.

In experimental studies Tian *et al* [3] have investigated the growth of Mn overlayers on a Pd(111) substrate using low-energy electron diffraction (LEED), Auger-electron low-energy spectroscopy, and ultraviolet photoemission spectroscopy. The studies showed that Mn films grown at room temperature had a strained fcc γ-Mn structure. In a subsequent paper Tian *et al* [4] investigated the growth of Mn films by epitaxy on Cu(111), finding a new metastable phase. They showed that the surface $(\sqrt{3} \times \sqrt{3})$R30° phase is in fact the bulk phase and is probably related to α-Mn. Grigorov and Walker [5] grew Mn/Cu multilayers on Cu(111) single crystals and monitored growth by *in situ* reflection high-energy electron diffraction. The magnetic properties were investigated using SQUID magnetometry in the temperature range 2 to 150 K. From the observations it was concluded that Mn is antiferromagnetic with a

transition temperature around or below 2 K. Subsequently Grigorov *et al* [6] used single-crystal x-ray diffraction and exchange bias measurements to study the 'expanded' (or $(\sqrt{3} \times \sqrt{3})R30°$ reconstructed) Mn phase deposited on (111)-orientated fcc noble metals including Cu(111) and Ag(111). This expanded phase was considered to be a trigonally distorted α-Mn structure on the basis of these measurements. Schneider *et al* [7] studied, using STM under UHV conditions, the interactions of Mn deposits with a Cu(111) substrate. They found the $(\sqrt{3} \times \sqrt{3})R30°$ superstructure on the atomic scale, and on a larger scale a hexagonal dislocation network which changes in order and periodicity with increasing annealing temperature. However, although their experiments deal with surface thicknesses of as little as 2 to 12 Å, this is somewhat thicker than the monolayers considered in this paper. In the monolayer limit, Mn forms a close-packed structure similar to γ-Mn, but as the layer thickness increases the film undergoes a $\sqrt{3} \times \sqrt{3}$ reconstruction or forms the so-called expanded phase mentioned above. Literature dealing with Cr on Cu(111) is rather sparse. Gaigher and van der Berg [8] have studied the orientation and morphology of Cr deposits on hot Cu(111) substrates. Transmission electron microscopy and electron diffraction were used as experimental probes. We refer the reader to their paper for a further discussion of Cr growth at various temperatures and thicknesses.

Methods based on local spin-density functional (LSDF) theory have been developed to a point where reliable predictions of the structural, electronic, and magnetic properties of thin films and surfaces are possible. Notably, predictions of magnetic moment enhancement on 3d-transition-metal surfaces or in ultrathin films deposited on non-magnetic substrates have been quite successful [9–13]. For geometries where the local atomic structure leads to a frustration of magnetic exchange interactions (e.g. at steps in γ-Fe films grown on Cu(100)), non-collinear magnetic structures have been predicted.

Very recently Asada *et al* [14] and Spišák and Hafner [15] conducted a systematic set of calculations on ultrathin antiferromagnetic films on (111) noble-metal substrates. The calculations of Asada *et al* used the full-potential linearized augmented-plane-wave (FLAPW) method adapted to the film geometry [16, 17]. Non-collinear magnetism is implemented using an atomic-sphere-like approximation with a fixed spin-quantization axes within muffin-tin spheres and a continuous vector spin density in the interstitial region. Spišák and Hafner used the linear muffin-tin orbital (LMTO) method in the atomic-sphere approximation (ASA) [18], where the spin-quantization axis is fixed within each sphere (there is no interstitial charge or spin density in the ASA). In both studies, ferromagnetic, row-wise antiferromagnetic, and $\pm 120°$ non-collinear configurations have been considered. Asada *et al* find the non-collinear magnetic arrangement to be the ground state for Cr on Cu(111), while for Mn on Cu(111) the ground state appears to be a collinear antiferromagnetic arrangement. Spišák and Hafner on the other hand find the non-collinear magnetic structure to be 2 meV lower in energy for Mn/Cu(111). In a further recent report, Kurz *et al* [19] extended the FLAPW studies to Cr and Mn monolayers on Ag(111) and reported results completely analogous to those obtained by Asada *et al* on Cu(111). The discrepancy between the two sets of results can be attributed to two different reasons:

 (i) The investigations of Asada *et al* [14] and Kurz *et al* [19] are performed in the local density approximation (LDA), whereas Spišák and Hafner [15] used the generalized-gradient approximation (GGA) in the exchange–correlation functional. It is well known that the use of the GGA is mandatory for a correct description of the magnetic ground state of bulk Cr, Mn, and Fe [13, 20, 21], although the influence appears to be somewhat less pronounced in thin films [13].

 (ii) The direction of magnetization changes discontinuously from site to site in the ASA, whereas the approach used by Asada *et al* allows for a gradual reorientation in the interstitial region.

However, both investigations neglect the fact that in any case the magnetic configuration breaks the symmetry of the (111) surface. In our recent study [22] of small magnetic clusters, we find that for triangular Fe_3 and Cr_3 clusters, Wannier's [2] result that the magnetic ground state is non-collinear is circumvented because the structure relaxes away from the equilateral triangle thus allowing a collinear antiferromagnetic ground state to be formed. In the current paper we use a fully unconstrained approach based on the LDA + GGA and the projector-augmented-wave (PAW) technique [23, 24] in which the direction of the magnetization is a continuous variable of position and which allows the simultaneous relaxation of the atomic and magnetic structures. Section 1 contains a brief description of the theory. In section 2 we briefly discuss the implementation of the current calculations. Section 3 discusses the structural, electronic, and magnetic properties of free-standing triangular Cr and Mn monolayers and of monolayers adsorbed on Cu(111) surfaces. Finally, section 4 contains a brief summary of our main conclusions.

2. LSDF theory for non-collinear spin structures

A generalization of von Barth and Hedin's [25] local spin-density functional (LSDF) theory to non-collinear magnetism was first proposed by Kübler *et al* [26, 27] within the framework of the augmented-spherical-wave (ASW) method and the atomic-sphere approximation. The effective single-particle equations for non-collinear magnets were derived by allowing the spin-quantization axis to vary from site to site in crystalline systems. The orientation of the axis with respect to the reference frame is a property of the ground state. They predicted well defined sets of directions for the spins, which are uncoupled from the crystal lattice unless spin–orbit coupling effects are included in the Hamiltonian (even though such effects are small in comparison to the spin–spin interactions).

Following Kübler *et al* [26, 27], spin-polarized density functional theory is expressed in terms of a 2×2 density matrix with elements $n^{\alpha\beta}(r)$. The electron density is then

$$\text{Tr}\left[n^{\alpha\beta}(r)\right] \equiv n_{\text{Tr}}(r) = \sum_{\alpha} n^{\alpha\alpha}(r). \tag{1}$$

The total-density matrix may then be defined as

$$n^{\alpha\beta}(r) = (n_{\text{Tr}}(r)\delta_{\alpha\beta} + \vec{m}(r) \cdot \vec{\sigma}^{\alpha\beta})/2. \tag{2}$$

In addition, for the density matrix, we can make a transformation to the equivalent magnetization density using the following formula†:

$$\vec{m}(r) = \sum_{\alpha\beta} n^{\alpha\beta}(r) \cdot \vec{\sigma}^{\alpha\beta} \tag{3}$$

where $\vec{\sigma} = (\sigma_x, \sigma_y, \sigma_z)$ are the Pauli spin matrices. The exact Kohn–Sham density functional becomes (we use atomic units, $\hbar = m = e^2 = 1$)

$$E = \sum_{\alpha} \sum_{n} f_n \langle \Psi_n^{\alpha} | -\frac{1}{2}\Delta | \Psi_n^{\alpha} \rangle + E_H[n_{\text{Tr}} + n_Z] + E_{xc}[n^{\alpha\beta}]. \tag{4}$$

$E_H[n_{\text{Tr}} + n_Z]$ is the electrostatic energy of the electronic charge density n_{Tr} and the point charge densities of the nuclei n_Z and is defined by

$$E_H[\wp] = \frac{1}{2} \int \int \frac{\wp(r)\wp(r')}{|r - r'|} \, dr \, dr' \tag{5}$$

where $\wp = n_{\text{Tr}} + n_Z$. $E_{xc}[n^{\alpha\beta}]$ is the electronic exchange–correlation energy and f_n are orbital occupation numbers. The exchange–correlation energy is not known in general, but

---

† The magnetization density is calculated from the spin density defined here, by multiplying by the factor $e\hbar/mc$.

only for a spin-polarized homogeneous electron gas with charge density n_{Tr} and magnetization density $\vec{m}$. In the local spin-density approximation, $E_{xc}[n^{\alpha\beta}]$ is defined by

$$E_{xc}[n^{\alpha\beta}] = \int n_{\text{Tr}}(r)\epsilon_{xc}[n^{\alpha\beta}(r)] \, \mathrm{d}r = \int n_{\text{Tr}}(r)\epsilon_{xc}[n_{\text{Tr}}(r), |\vec{m}(r)|] \, \mathrm{d}r. \quad (6)$$

The exchange–correlation functional leads to the non-magnetic scalar exchange–correlation potential:

$$v_{xc}\left[n^{\alpha\beta}\right](r) = \frac{\delta E_{xc}[n^{\alpha\beta}]}{\delta n_{\text{Tr}}(r)} = \epsilon_{xc}[n^{\alpha\beta}(r)] + n_{\text{Tr}}(r)\frac{\partial\epsilon_{xc}[n^{\alpha\beta}(r)]}{\partial n_{\text{Tr}}(r)} \quad (7)$$

and to the magnetic exchange–correlation field:

$$\vec{b}\left[n^{\alpha\beta}\right](r) = \frac{\delta E_{xc}[n^{\alpha\beta}]}{\delta\vec{m}(r)} = \frac{\partial|\vec{m}(r)|}{\partial\vec{m}(r)}\frac{\delta E_{xc}[n^{\alpha\beta}]}{\delta|\vec{m}(r)|} = \hat{m}(r)n_{\text{Tr}}(r)\frac{\partial\epsilon_{xc}[n^{\alpha\beta}(r)]}{\partial|\vec{m}(r)|} \quad (8)$$

where

$$\hat{m}(r) = \frac{\partial|\vec{m}(r)|}{\partial\vec{m}(r)} \quad (9)$$

is the direction of the magnetization density at the point r. The potential $\vec{b}(r)$ is parallel to the magnetization density $\vec{m}(r)$ everywhere. The actual functional form of ϵ_{xc} can be parametrized in several ways. At the level of the local density approximation, we used the exchange–correlation functional proposed by Perdew and Zunger [28] based on the quantum Monte Carlo simulations of Ceperley and Alder [29] for the interacting electron gas. For the intermediate spin polarizations we used the interpolation proposed by von Barth and Hedin [25]. The generalized-gradient approximation (GGA) has been developed with the aim of incorporating the leading non-local corrections to the LDA. In the GGA, the exchange–correlation functional depends also on the absolute values of the gradients of charge and spin density. Out of the many different GGA functionals proposed in the literature, we choose the form proposed by Perdew *et al* [30]; the approach of White and Bird [31] has been used to calculate the spin-polarized GGA potentials.

The projector-augmented-wave (PAW) method [23, 24] is an all-electron method for electronic structure, total-energy, and force calculations which is closely related to the ultrasoft-pseudopotential technique [32, 33]. In the PAW approach, charge and spin densities are decomposed into pseudo-densities and compensation densities accounting for the difference between the pseudo-densities and all-electron densities. The pseudo-densities consist of a smooth part expressed in a plane-wave representation and localized augmentation charges accounting for the violation of norm conservation [32, 33]. Both augmentation and compensation charges are represented on radial support grids. For each of the atom-centred radial support grids the spin-quantization axis is fixed—in this respect our approach resembles the unconstrained non-collinear FLAPW technique used by Asada *et al* [14], but unlike in the FLAPW method, in the PAW approach the plane-wave description is not restricted to the interstitial region, but extends over the complete volume of the system. Hence variations of the magnetization direction are allowed also within the augmentation spheres. For a detailed discussion of the non-collinear PAW formalism we refer the reader to Hobbs *et al* [22].

3. Methodology

Our calculations adopt periodic boundary conditions but retain a vacuum of width 8.4 Å in the z-direction to reduce the interactions in this direction between the periodic images to negligible proportions. Our structure consists either of a single Cr or Mn monolayer or of five substrate

layers of copper atoms and one surface layer of either Cr or Mn. The copper substrate is firstly relaxed using a k-point mesh of $15 \times 15 \times 1$. The relaxed substrate is then used in subsequent calculations. For the collinear magnetic calculations we have compared our results for k-point meshes of $8 \times 8 \times 1$ and $12 \times 12 \times 1$. The magnetic energy difference is ~ 3.5 meV and the magnetic moments change by ~ 0.05 μ_B. The thin-film results presented in this paper use the $8 \times 8 \times 1$ mesh which as mentioned above should have an error in magnetic energy of around 3.5 meV. As the unit cell used for the non-collinear calculations is larger, one would expect the errors due to k-point density to be somewhat smaller in this case. In the calculations dealing with adsorbed monolayers we relax the three uppermost substrate layers and the surface layer. For the calculations on the free-standing monolayers a structural relaxation affects only the bond length within the plane and we have calculated the magnetic moment and total energy as functions of the interatomic distance to determine the energy minimum.

All calculations have been performed using the PAW [23, 24] method, using a cut-off of 270 eV for the plane-wave basis set and incorporating the generalized-gradient approximation. The collinear calculations rely on the LSDF theory of von Barth and Hedin [25]. Non-collinear calculations utilize our recently developed fully unconstrained approach in which the magnetization density is a continuous variable of position [22]. The method allows both the atomic and magnetic structures to relax simultaneously and self-consistently.

4. Structural and magnetic properties of triangular Cr and Mn monolayers

In the present calculations we consider:

 (1) the ferromagnetic p(1×1) structure with one surface atom in the two-dimensional unit cell,
 (2) the collinear row-wise antiferromagnetic structure with c(2×2) periodicity and two atoms in the unit cell (see figure 1(b)), and
 (3) the non-collinear 120° configuration of nearest-neighbour moments with a $(\sqrt{3} \times \sqrt{3})$R30° unit cell containing three surface atoms.

Figure 1(a) shows the latter structure. Unlike in the planar ferromagnetic model, where only global spin-rotation symmetry is broken, an additional reflection symmetry is broken in this case (see Lee *et al* [1] for a description). Figure 1 indicates two topologically distinct patterns, characterized by different helicities and indicated by '+' and '−' symbols. Each elementary triangle is assigned a helicity according to the way the three spins at the vertices of the triangle are aligned. A positive (+) helicity describes an arrangement in which the spins are rotated sequentially by 120° clockwise when the triangle is traversed in a clockwise direction while a negative (−) helicity refers to anticlockwise rotations traversing the triangle in a clockwise direction. In the collinear antiferromagnetic c(2×2) structure the C_{3v} symmetry is broken; nearest-neighbour bonds between ferromagnetically coupled atoms along the rows of parallel spins are no longer equivalent to bonds between antiferromagnetically coupled atoms. In the following we shall first discuss the properties of free-standing monolayers.

4.1. Free-standing triangular Cr and Mn monolayers

Figure 2 summarizes our results for the magnetic moments and total energies of the three possible magnetic configurations as functions of the nearest-neighbour bond length. In both Cr and Mn monolayers, a ferromagnetic high-spin phase with a magnetic moment of nearly 4 μ_B is stable only at expanded interatomic distances. In Cr monolayers the magnetic moment breaks down rather suddenly at a bond length of about 2.57 Å, the ferromagnetic
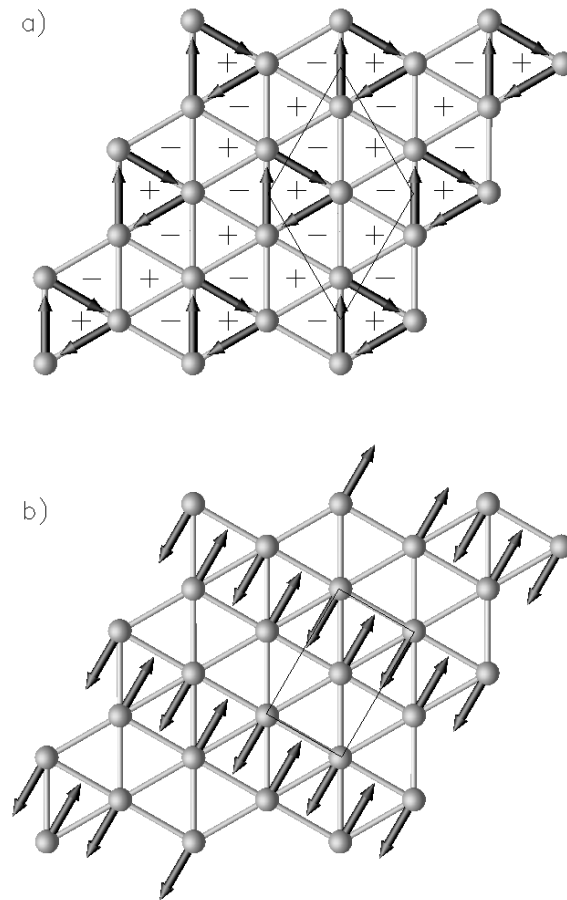
Figure 1. (a) Non-collinear magnetic structure of triangular layers corresponding to the frustrated XY-models with nearest-neighbour interactions. The relative directions of the magnetic moments (neglecting spin–orbit coupling) are indicated by the arrows. + and − signs indicate the helicities assigned to the elementary triangles (see the text). The primitive ($\sqrt{3} \times \sqrt{3}$) unit cell is indicated by the thin lines. (b) Row-wise antiferromagnetic structure of triangular layers. Arrows indicate the relative directions of the magnetic moments; the thin lines show the c(2×2) unit cell.

minimum being about 280 meV higher in energy than the non-magnetic minimum. In Mn monolayers we find a transition from a ferromagnetic high-spin phase at bond lengths larger than 2.47 Å to a ferromagnetic low-spin phase at closer interatomic distances. The low-spin phase ($M \leqslant 1.5 \mu_B$) loses its magnetic moment only at strongly reduced bond lengths.

The row-wise antiferromagnetic c(2×2) Cr monolayer has an equilibrium bond length of 2.70 Å at a magnetic moment of 3.75 μ_B. Under compression the magnetic moment is strongly reduced; it disappears at a bond length of 2.31 Å corresponding roughly to the bond length of the non-magnetic phase. The non-collinear 120° phase represents the magnetic ground state (the magnetic energy differences are summarized in table 3, later); the equilibrium bond length is about 2.65 Å. At these distances, the magnetic moment is slightly smaller than in the antiferromagnetic phase. Under compression, the non-collinear magnetic moments are gradually reduced. They disappear at distances somewhat smaller than the equilibrium distances in the non-magnetic phase.
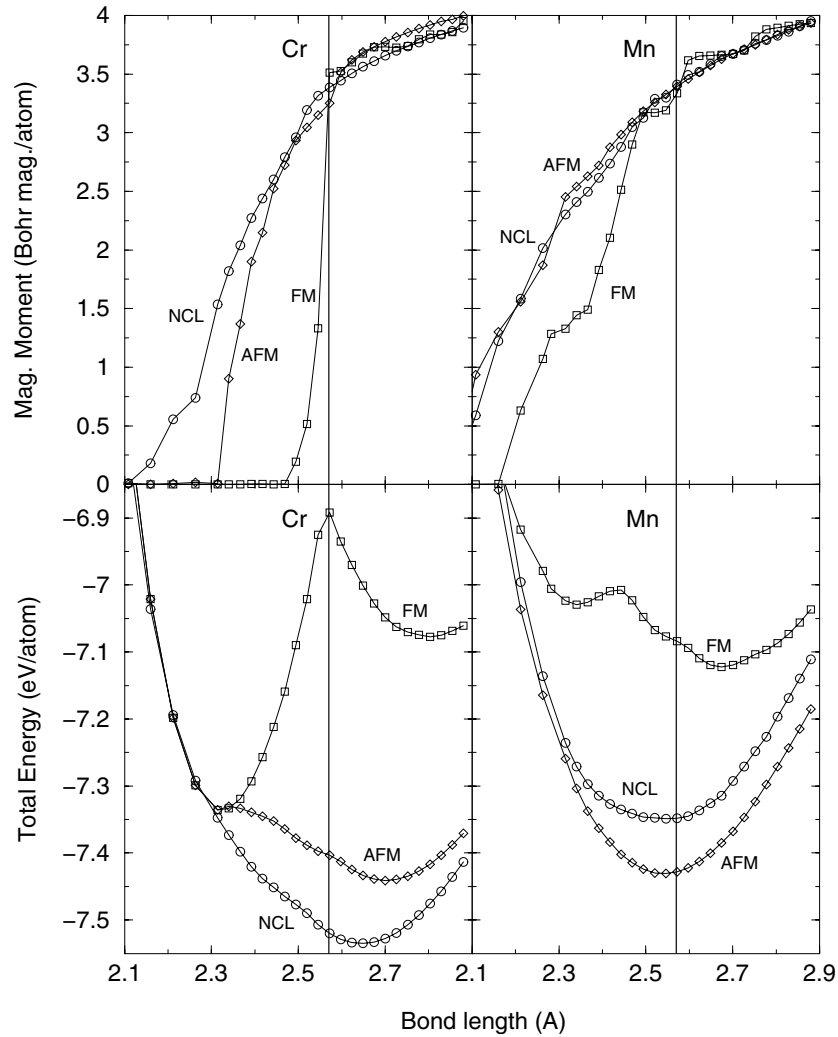
Figure 2. Total energy and magnetic moments of the ferromagnetic p(1 × 1), the antiferromagnetic c(2 × 2), and the non-collinear ($\sqrt{3} \times \sqrt{3}$) phases of free-standing triangular Cr and Mn monolayers as functions of the nearest-neighbour bond length. The vertical lines mark the lateral interatomic distance of a Cu(111) substrate.

In Mn monolayers the relative stability of the antiferromagnetic and non-collinear phase is reversed (see table 3, later, and figure 2), the equilibrium bond lengths and magnetic moments being almost the same in the two phases. Under compression the magnetic energy difference is quickly reduced; at bond lengths smaller than about 2.35 Å, the two phases are energetically almost degenerate.

4.2. Triangular Cr and Mn overlayers on Cu(111)

The results for overlayers adsorbed on Cu(111) substrates are summarized in tables 1 and 2. Again the same three magnetic configurations have been considered. The calculations have been performed with a fixed lateral interatomic distance of 2.57 Å corresponding to the

Table 1. Calculated atomic magnetic moments M_{At} (in μ_B/atom), magnetic energy differences ΔE_{Tot} (in meV/atom), and percentage changes Δd_{ij} in the interlayer separation for Cr on Cu(111). NCL, FM, AFM, and NM correspond to non-collinear, ferromagnetic, antiferromagnetic, and non-magnetic starting configurations. For the non-collinear calculations the three Cartesian components of the atomic magnetic moments are listed.

Calculation (initial magnetic configuration)	M_{At}	ΔE_{Tot}	Δd_{ij} (%)				
			Δd_{12}	Δd_{23}	Δd_{34}	Δd_{45}	Δd_{56}
(1×1) (FM)	Cr(1) $\Rightarrow$ +0.03	52.0	+0.31	+0.15	−0.70	−1.55	−0.75
	Cu(x) $\Rightarrow$ +0.00						
$c(2 \times 2)$ (AFM)	Cr(1) $\Rightarrow$ +2.76	13.4	+2.66	−0.14	−0.96	−1.62	−0.75
	Cr(2) $\Rightarrow$ −2.76						
	Cu(3) $\Rightarrow$ +0.01						
	Cu(4) $\Rightarrow$ −0.01						
	Cu(x) $\Rightarrow$ +0.00						
$c(2 \times 2)$ (AFM)*	Cr(1) $\Rightarrow$ +2.76	13.3	+2.40	−0.32	−1.07	−1.66	−0.75
	Cr(2) $\Rightarrow$ −2.77		+3.19	+0.03	−0.72	−1.36	−0.75
	Cu(3) $\Rightarrow$ +0.01						
	Cu(4) $\Rightarrow$ −0.01						
	Cu(x) $\Rightarrow$ +0.00						
$(\sqrt{3} \times \sqrt{3})$ (NCL)	Cr $\Rightarrow$ −2.49, −1.44, −0.01	0.0	+3.13	0.16	−0.78	−1.28	−0.75
	$\Rightarrow$ −0.00, +2.88, −0.01						
	$\Rightarrow$ +2.49, −1.44, −0.01						
	Cu $\Rightarrow$ +0.00, +0.00, +0.00						

* Allowing in-plane distortion.

Table 2. Calculated atomic magnetic moments M_{At} (in μ_B/atom), magnetic energy differences ΔE_{Tot} (in meV/atom), and percentage changes Δd_{ij} in the interlayer separation for Mn on Cu(111). The format is the same as in table 1.

Calculation (initial magnetic configuration)	M_{At}	ΔE_{Tot}	Δd_{ij} (%)				
			Δd_{12}	Δd_{23}	Δd_{34}	Δd_{45}	Δd_{56}
(1×1) (FM)	Mn(1) $\Rightarrow$ +2.77	50.0	+1.33	−0.11	−0.75	−1.66	−0.75
	Cu(1) $\Rightarrow$ +0.03						
	Cu(x) $\Rightarrow$ −0.01						
$c(2 \times 2)$ (AFM)	Mn(1) $\Rightarrow$ +3.19	0.0	+2.29	−0.20	−1.02	−1.47	−0.75
	Mn(2) $\Rightarrow$ −3.19						
	Cu(3) $\Rightarrow$ +0.02						
	Cu(4) $\Rightarrow$ −0.02						
	Cu(x) $\Rightarrow$ +0.00						
$c(2 \times 2)$ (AFM)*	Mn(1) $\Rightarrow$ +3.18	0.0	+1.68	−0.24	−1.10	−1.52	−0.75
	Mn(2) $\Rightarrow$ −3.19		+2.67	−0.07	−0.85	−1.34	−0.75
	Cu(3) $\Rightarrow$ +0.02						
	Cu(4) $\Rightarrow$ −0.02						
	Cu(x) $\Rightarrow$ +0.00						
$(\sqrt{3} \times \sqrt{3})$ (NCL)	Mn $\Rightarrow$ −2.80, −1.56, +0.08	11.5	+2.85	+0.33	−0.68	−1.15	−0.75
	$\Rightarrow$ +0.00, +3.16, +0.08						
	$\Rightarrow$ +2.61, −1.83, +0.10						
	Cu $\Rightarrow$ +0.00, +0.00, +0.00						

* Allowing in-plane distortion.

equilibrium lattice constant of Cu calculated in the GGA. Only for the antiferromagnetic $c(2 \times 2)$ phase have we in addition performed calculations allowing for an optimization of the

distances between ferromagnetically and antiferromagnetically coupled atoms in the adsorbed layer. For comparison, the vertical lines in figure 2 show the lateral lattice constant of the Cu(111) substrate. We find that triangular Mn layers show an almost ideal epitaxial match to the substrate, whereas adsorbed Cr layers undergo a small compressive strain.

Ferromagnetism is unstable in Cr overlayers—this is not surprising since the interatomic distance imposed by the epitaxial constraint corresponds exactly to the distance where the ferromagnetism of a free monolayer breaks down. In both the antiferromagnetic and the non-collinear phases, the magnetic moments are reduced compared to those of the free-standing monolayer. This reduction is distinctly larger than that expected from the epitaxial mismatch. The reason for this is that the hybridization of the Cu and Cr 3d bands at the interface leads to a broadening of the Cr 3d band and further to the observed additional reduction of exchange splitting and magnetic moment. Structural relaxation effects are weak, except for a slight outward relaxation of the Cr overlayer and an even smaller contraction of the Cu–Cu interlayer distances closest to the Cr–Cu interface. The in-plane distortion of the antiferromagnetic c(2 × 2) phase induced by the inequivalence of the bond length in ferromagnetic and antiferromagnetic nearest-neighbour pairs is only 0.4%, i.e. at the limit of the computational accuracy. The magnetic energy differences of free-standing and adsorbed Cr monolayers are compared in table 3; that between the collinear antiferromagnetic and non-collinear phase is only slightly reduced by the interaction with the substrate.

Table 3. Differences in total energy ΔE_{Tot} (in meV/atom) relative to the ground state and calculated assuming that the substrate has no effect on magnetic energy differences in Cr and Mn.

Atom type	Calculation	ΔE_{Tot} for monolayer	$\Delta E_{Tot} \times 6$ for ad-layer
Cr	(1 × 1) (FM)	457.9	312.0
	c(2 × 2) (AFM)	94.1	80.4
Mn	(1 × 1) (FM)	308.2	300.0
	($\sqrt{3} \times \sqrt{3}$) (NCL)	81.8	69.0

In Mn overlayers a reduction of the magnetic moment comparable to that found in Cr/Cu(111) is found only for the ferromagnetic phase; in the antiferromagnetic and non-collinear phases the reduction is smaller than 10%. This is as expected, since in this case the reduction is caused solely by the d-band hybridization across the interface. The relaxation of the interlayer distances is almost the same as for Cr adlayers. Only the in-plane distortion of the antiferromagnetic c(2 × 2) phase is slightly more pronounced. However, this distortion is too small to have any influence on the magnetic energy differences. In the non-collinear case for manganese, the magnetic moments are slightly asymmetric, of the order of ∼1%. This is probably caused by the extremely slow convergence in this metastable state. Both the ferromagnetic/antiferromagnetic and the non-collinear/antiferromagnetic energy differences are slightly reduced through the interaction with the substrate. The important point is that for Mn/Cu(111) the antiferromagnetic phase remains energetically favoured.

4.3. Magnetization densities

In the following we analyse in detail the variation of the magnetization densities in the magnetically frustrated monolayers. Figure 3 shows the magnetization density calculated for the non-collinear phase of Cr on Cu(111). The local direction of the magnetic moment is indicated by the arrows, the length of the arrows being proportional to the absolute value of the magnetization density. In addition, around each site iso-surfaces of the magnetization densities
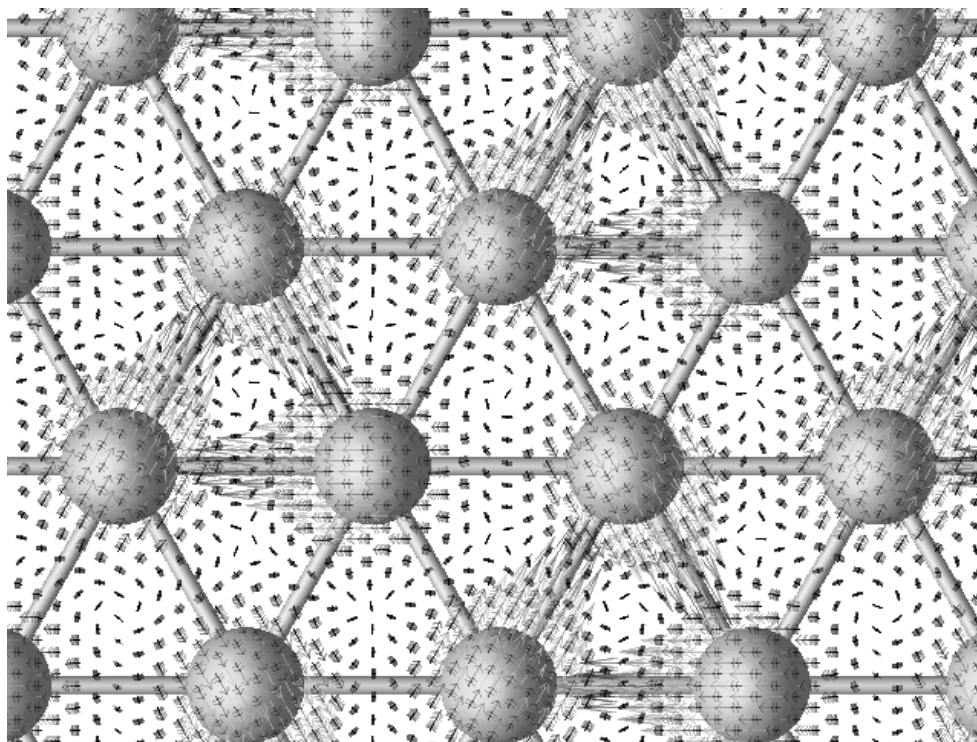
Figure 3. The vector field of the magnetization density for the non-collinear phase of Cr on Cu(111). The relative direction of the magnetization density (neglecting spin–orbit coupling) is indicated by the arrows; the length of each arrow is proportional to the absolute value of the local magnetization density.

are drawn. At a first look one tends to conclude that the magnetization densities are fairly well localized and, as the iso-surfaces are also almost spherical at reasonably large values, the conclusion that the ASA is a reasonable choice in this system seems to be appropriate. However, the regions around the atoms in which the direction of magnetization is approximately constant are distinctly smaller than the muffin-tin spheres of the FLAPW method or the overlapping atomic spheres of the LMTO approach. Interesting new aspects of this study are seen precisely in the bonding and interstitial regions where the direction of the magnetization changes.

In figure 3 we recognize characteristic patterns in the vector field of the magnetization density: inside the elementary triangles to which a positive helicity has been assigned, the vector field forms a vortex which may be a clockwise or an anticlockwise spiral or show a circular pattern; inside the triangles with negative helicity we find anti-vortex patterns related to each other by 120° rotations. Detailed views of the three types of vortex are shown in figures 4, 5, and 6. Spiral vortices are formed inside the triangles where the direction of the magnetization is aligned (for the given alignment of the magnetization directions with respect to the crystal lattice) along the bond directions, pointing either away from or into the triangle. In both cases the direction of magnetization in the bond centres is perpendicular to the bonds; in the former case the vectors point out of the triangle and an outward spiral is formed (figure 4), while in the latter case the vectors point towards the centre of the triangle such that an inward spiral is formed (figure 5). A circular vortex is formed within those triangles where the magnetization at the lattice sites is perpendicular to one of the edges of
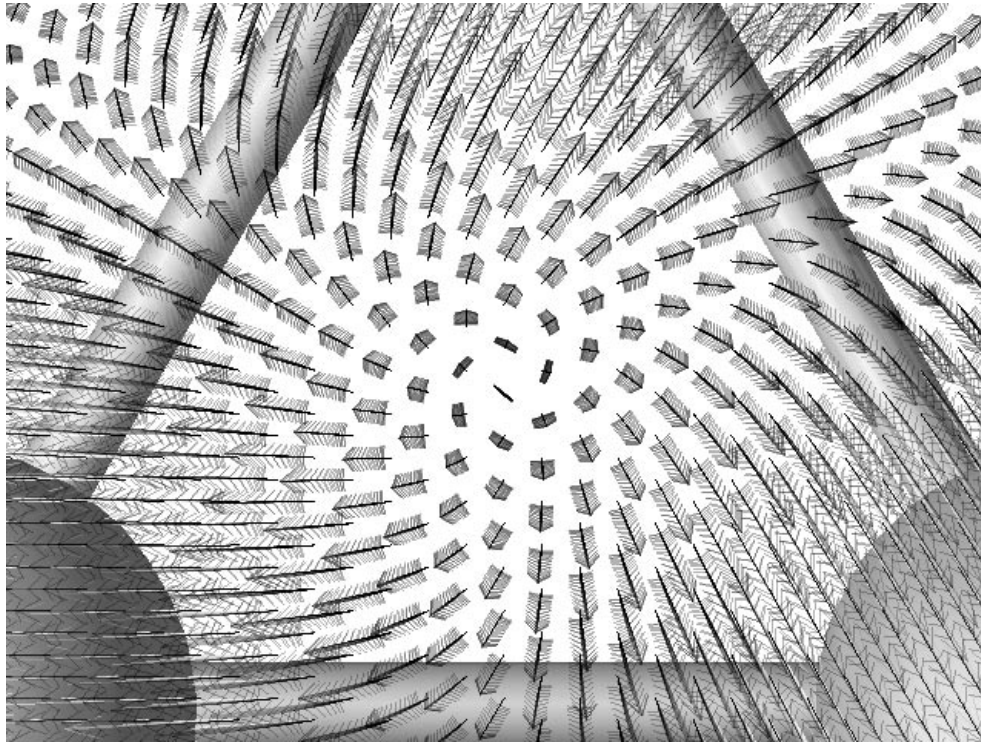
Figure 4. An enlarged view of a vortex of the magnetization with an out-flowing spiral structure within an elementary triangle with positive helicity. See the text.

the triangle. In the bond centres, the magnetization is in this case aligned along the bond directions (figure 6). An example of an anti-vortex structure realized in triangles with negative helicity is shown in figure 7. In this case the direction of magnetization is perpendicular to two of the bonds (pointing either out of or into the triangle) and parallel to the third bond. To the three different types of vortex correspond anti-vortex structures rotated by 120°. The information on the structure of the magnetic flux lines in the interstitial regions is summarized in figure 8. It is easy to verify that the vortex/anti-vortex structure is invariant under a global rotation of the vector field of the magnetization with respect to the planar lattice of the magnetic layer.

This picture also illustrates an important difference between the muffin-tin-like description of the magnetization density within the FLAPW approach used by Asada *et al* [14] and Kurz *et al* [19] and the present PAW description. In the FLAPW approach, the direction of magnetization changes discontinuously at the spheres' boundary. In the PAW description, the direction of magnetization changes continuously and is (for the present choice of the global alignment) at these points either parallel or perpendicular to the bond, depending on its local environment. It is also interesting to note that the bond centres form a Kagomé lattice dual to the triangular lattice of the atoms. The six triangles surrounding a hexagon of the Kagomé lattice contain an alternating anti-vortex or vortex, the existence of three different types leading to further symmetry breaking analogous to the positive and negative helicities. This point certainly deserves further investigation.
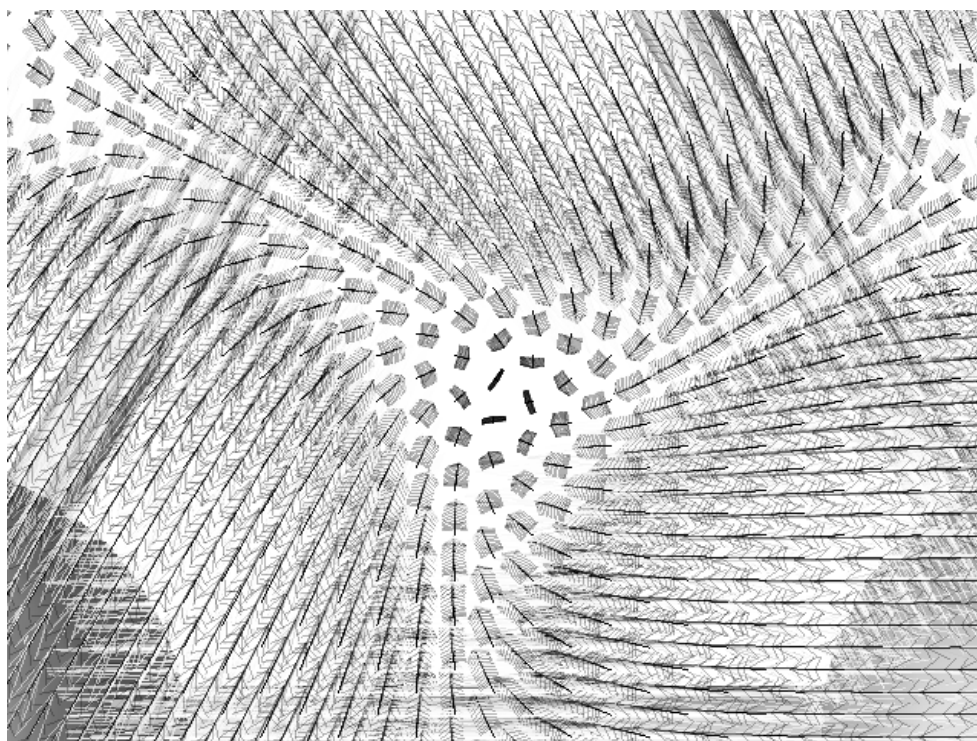
Figure 5. An enlarged view of a vortex of the magnetization density with an in-flowing spiral structure within a triangle with positive helicity. See the text.

Finally, we have also analysed the magnetization density of the row-wise antiferromagnetic structure (see figure 9), which demonstrates that the magnetization density changes direction through zero at an invariant orientation in the boundary between the 'spin-up' and 'spin-down' regions.

5. Discussion and summary

In this paper we have performed self-consistent *ab initio* local spin-density calculations of the magnetic ground states in triangular free-standing monolayers of Cr and Mn and of Cr and Mn overlayers on a Cu(111) substrate. Our approach uses the projector-augmented-wave method with generalized-gradient corrections. The non-collinear calculations use our newly developed fully unconstrained description of the magnetization density which allows the atomic, electronic, and magnetic structures to be relaxed simultaneously and self-consistently. The magnetization density is treated as a continuous vector variable of position.

For Cr we find that the ground state is non-collinear for both the free-standing and adsorbed monolayers. However, in the case of Mn the ground state was clearly found to be collinear antiferromagnetic. Such a situation is surprising as it seems to contradict the prediction based on the analysis of the frustrated triangular antiferromagnetic XY-model [1] that the ground state of a triangular layer with predominantly antiferromagnetic interactions has the $\pm120°$ non-collinear configuration. Our fully unconstrained results calculated using the PAW method agree with the FLAPW results of Asada *et al* [14] who implemented the
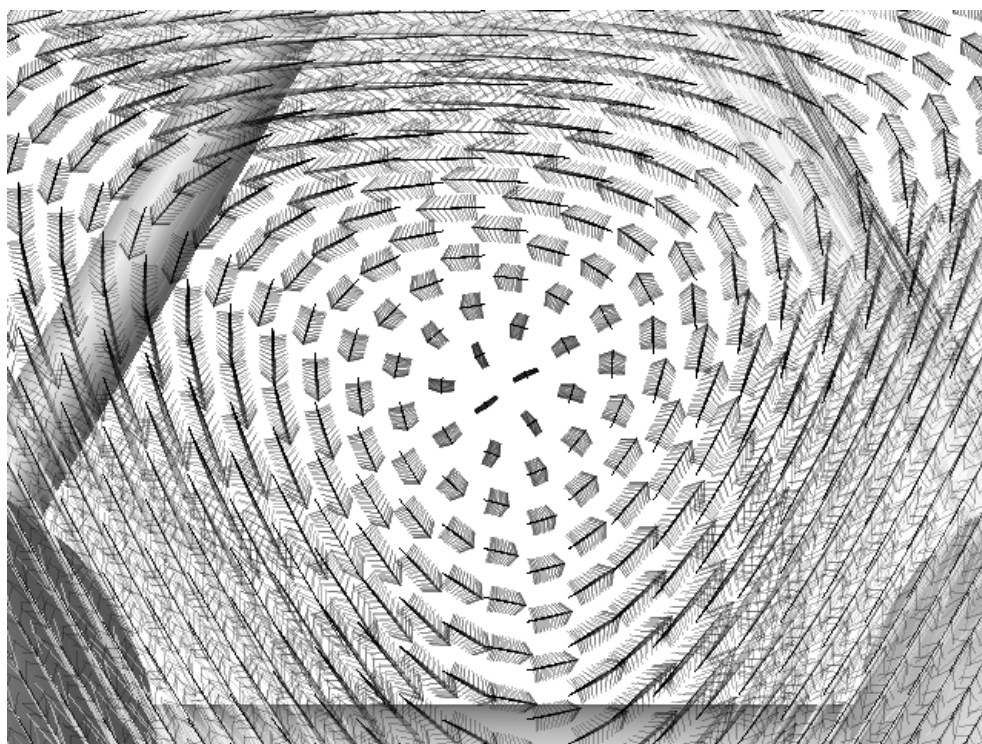
Figure 6. An enlarged view of a vortex of the magnetization density with a circular structure within a triangle with positive helicity. See the text.

unconstrained approach only in the interstitial regions and used fixed quantization axes in the muffin-tin regions. Asada *et al* [14] have primarily considered unsupported monolayers of Cr and Mn but have repeated the calculation for Mn on a five-layer Cu(111) slab. Our results disagree with the recent calculation of Spišák and Hafner [15] predicting almost equal magnetic energies for the collinear antiferromagnetic and non-collinear phases of Mn/Cu(111) using an LMTO-ASA approach with fixed magnetization direction within each atomic sphere. The comparison of these three sets of calculations clearly emphasizes the importance of an unconstrained description of the magnetization densities—for itinerant magnets, the ASA approach to non-collinear magnetism is found to be of limited validity in the present case. Of course it is conceivable that under favourable experimental conditions, interdiffusion leads to the formation of a surface alloy. However, this case is not discussed here, because the Mn–Mn interactions in a surface alloy are certainly ferromagnetic, possible antiferromagnetism in alloys with more than two monolayers being of a layered type. No non-collinear structures are expected.

The difference in behaviour of triangular layers of Cr and Mn is clearly related to the rather long-range nature of the exchange interactions in the Mn layers, as already pointed out by Spišák and Hafner. In the non-collinear phase, first and third neighbours carry magnetic moments with a relative 120° orientation, but second-neighbour moments are ferromagnetically aligned (see figure 1). In the row-wise antiferromagnetic structure, out of six nearest- and next-nearest-neighbour atoms four are aligned antiferromagnetically and two ferromagnetically in each shell. All six sites in the third-neighbour shell show ferromagnetic alignment. If the
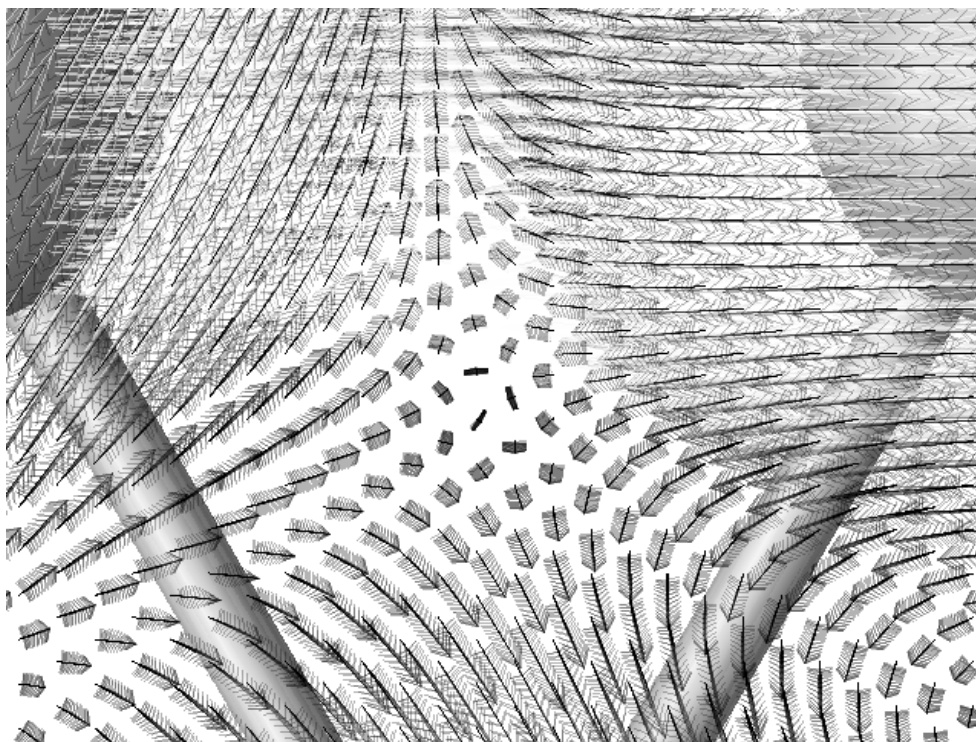
Figure 7. An enlarged view of an anti-vortex of the magnetization density within an elementary triangle with negative helicity. See the text.
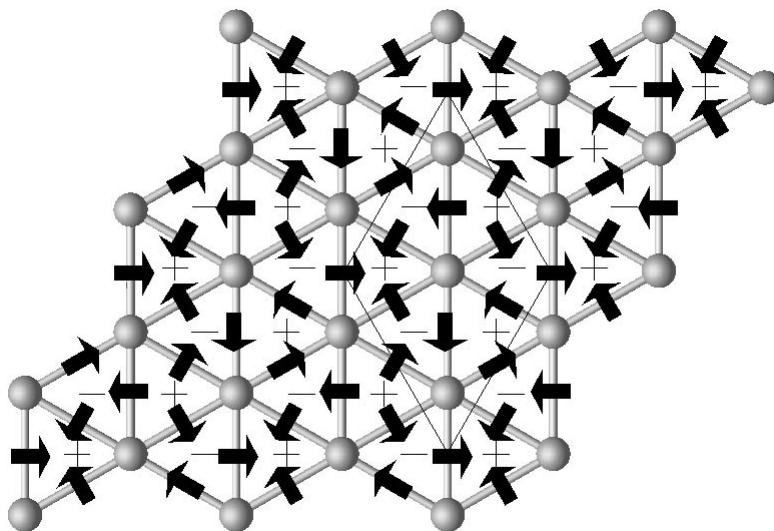

Figure 8. An illustration of the direction of magnetic flux lines of the non-collinear 120° phase as they intersect the bonds within the magnetic monolayer. Three distinct types of vortex are required to construct the diagram, namely an in-flowing spiral, an out-flowing spiral, and a circular vortex. The anti-vortices are formed in the remaining spaces by the interactions of the three types of vortex and exhibit threefold rotation symmetry.
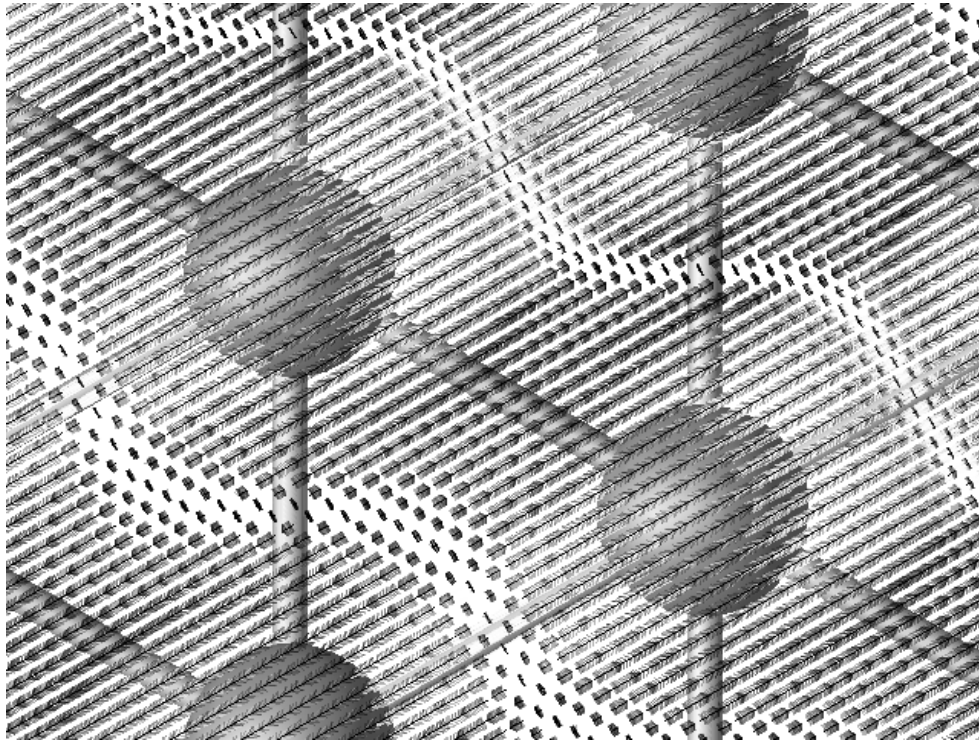
Figure 9. The vector field of the magnetization density for the row-wise antiferromagnetic $c(2 \times 2)$ phase of Mn on Cu(111). The arrows illustrate the directions of the magnetization, the length of each arrow being proportional to the absolute value of the local magnetization density. See the text.

exchange interaction is antiferromagnetic for the first two shells and ferromagnetic for the third shell, the frustration may be weaker in the collinear phase

We have also presented a detailed analysis of the magnetization densities in the interstitial regions. This analysis clearly confirms the importance of relaxing the magnetization directions. We have identified interesting symmetries in the vector field of the magnetization densities, with three different types of vortex structure in the elementary triangles with positive helicity and anti-vortices in the triangles with negative helicities. The existence of these three vortex types demonstrates that the formation of a non-collinear magnetic structure in an itinerant system leads to a new type of broken symmetry unknown in the localized spin models.

Acknowledgments

References

[1] Lee D H, Joannopoulos J D, Negele J W and Landau D P 1986 *Phys. Rev.* B **33** 450
[2] Wannier G H 1950 *Phys. Rev.* **79** 357
[3] Tian D, Li H, Wu S C, Jona F and Marcus P M 1992 *Phys. Rev.* B **45** 3749

[4]   Tian D, Begley A M and Jona F 1992 *Surf. Sci. Lett.* **273** L393
[5]   Grigorov I L and Walker J C 1997 *J. Appl. Phys.* **81** 3907
[6]   Grigorov I L, Walker J C, Hawley M E, Brown G W, Lütt M and Fitzsimmons M R 1998 *J. Appl. Phys.* **83** 7010
[7]   Schneider J, Rosenhaln A and Wandelt K 1999 *Appl. Surf. Sci.* **142** 68
[8]   Gaigher H L and van der Berg N G 1987 *Thin Solid Films* **146** 299
[9]   Fu C L, Freeman A J and Oguchi T 1985 *Phys. Rev. Lett.* **54** 2700
[10] Lorenz R and Hafner J 1996 *Phys. Rev.* B **54** 15937
[11] Spišák D and Hafner J 1997 *Phys. Rev.* B **55** 8304
      Spišák D and Hafner J 1997 *Phys. Rev.* B **56** 2646
[12] Moroni E G, Kresse G and Hafner J 1999 *J. Phys.: Condens. Matter* **11** L35
[13] Eder M, Moroni E G and Hafner J 1999 *Surf. Sci. Lett.* **243** L244
      Eder M, Moroni E G and Hafner J 2000 *Phys. Rev.* B **61** 11 492
[14] Asada T, Bihlmayer G, Handschuh S, Heinze S, Kurz Ph and Blügel S 1999 *J. Phys.: Condens. Matter* **11** 9347
[15] Spišák D and Hafner J 2000 *Phys. Rev.* B **61** at press
[16] Wimmer E, Krakauer H, Weinert M and Freeman A J 1981 *Phys. Rev.* B **24** 864
[17] Weinert M, Wimmer E and Freeman A J 1982 *Phys. Rev.* B **26** 4571
[18] Skriver H 1984 *The LMTO Method* (Berlin: Springer)
[19] Kurz Ph, Bihlmayer G, Förster F, Blügel S and Nordström L 2000 Ψ_k *Newsletter* **38** 64
[20] Asada T and Terakura K 1993 *Phys. Rev.* B **47** 15992
[21] Moroni E G, Kresse G, Hafner J and Furthmüller J 1997 *Phys. Rev.* B **56** 15629
[22] Hobbs D, Kresse G and Hafner J 2000 *Phys. Rev.* B submitted
[23] Blöchl P 1994 *Phys. Rev.* B **50** 17953
[24] Kresse G and Joubert D 1999 *Phys. Rev.* B **59** 1758
[25] von Barth U and Hedin L 1972 *J. Phys. C: Solid State Phys.* **5** 1629
[26] Kübler J, Höck K H and Sticht J 1988 *J. Appl. Phys.* **63** 3482
[27] Kübler J, Höck K H, Sticht J and Williams A R 1988 *J. Phys. F: Met. Phys.* **18** 469
[28] Perdew J P and Zunger A 1981 *Phys. Rev.* B **23** 5048
[29] Ceperley D M and Alder B J 1980 *Phys. Rev. Lett.* **45** 566
[30] Perdew J P, Chevary J A, Vosko S H, Jackson K A, Pederson M R, Singh D J and Fiolhais C 1992 *Phys. Rev.* B **46** 6671
[31] White J A and Bird D M 1994 *Phys. Rev.* B **50** 4954
[32] Vanderbilt D 1990 *Phys. Rev.* B **41** 7892
[33] Kresse G and Hafner J 1994 *J. Phys.: Condens. Matter* **6** 8245